Chemical Science

ROYAL SOCIETY OF CHEMISTRY

EDGE ARTICLE

View Article Online
View Journal | View Issue

Cite this: *Chem. Sci.*, 2026, **17**, 5745

All publication charges for this article have been paid for by the Royal Society of Chemistry

Received 4th November 2025
Accepted 22nd January 2026

DOI: 10.1039/d5sc08539j

rsc.li/chemical-science

Superstructure-induced enhancement of solid-state triphenylacrylonitrile photochromism *via* a macrocycle-mediated blocking strategy

Meng-Hao Li, Hui Hui, Yan Wang and Ying-Wei Yang *

Developing materials with precisely tunable photochromic properties is crucial for innovative applications, and this requires rational design strategies to overcome photoisomerization constraints imposed by molecular stacking. Herein, we introduce a pillararene-based "blocker" strategy to mitigate π–π stacking of photoisomerizable molecules. The pillararene entity facilitates photochromic chromophore torsion by providing free volume and stabilizes photoisomerization products in conjunction with specific volatile organic compounds (VOCs) through supramolecular interactions. With this strategy, we obtain a solid-state photochromic material induced by VOCs, exhibiting reversible white-to-red color changes. This material's enhanced photochromic behavior, especially when exposed to oxygen-containing VOCs, such as CH_3OH, HCOOH, and ethyl acetate, expands its potential applications in UV printing, anti-counterfeiting, and multi-dimensional information encryption. Leveraging the pillar-shaped structure and molecular recognition abilities of pillararenes, this study offers a straightforward strategy for the design of multi-stimuli-responsive photochromic molecules and functional supramolecular macrocycles.

Introduction

Photochromic compounds have attracted significant attention in scientific research and technological applications owing to their reversible color changes upon light irradiation, making them essential optical functional materials.[1] This phenomenon typically stems from the light-induced interconversion between two or more metastable molecular isomers,[2] resulting in altered light absorption and emission properties. Common photochromic compounds, such as spirooxazines,[3] spiropyrans,[4] and diarylethenes,[5,6] are widely deployed in various fields, including optical information storage,[7–10] specialty inks and coatings,[11] and advanced smart optical devices (*e.g.*, photochromic lenses and glasses).[12] Among these, diarylethene derivatives are promising candidates, particularly for emerging applications including high-density optical data storage,[13] advanced bioimaging,[14] and nanoscale optoelectronics,[15] due to their readily tunable chemical structures. This tunability, facilitated by multiple substitution sites, enables the fine-tuning of some crucial properties, such as high thermal stability, strong environmental resistance, low background absorption, high cycling durability, light-response wavelength, and color-change rate.[10,15–17] On this basis, triphenylethylene derivatives, prepared by substituting a hydrogen atom on the diarylethene framework with an additional phenyl ring, exhibit excellent photochromic performance with high sensitivity and rapid response *via* reversible intramolecular ring-opening/closure reactions,[18–25] enabling significant progress in applications such as photo-induced deformation and information encryption. However, due to tight π–π stacking during molecular aggregation, which impedes photocyclization, the photochromic behavior of these molecules remains significantly challenging in the solid state,[2,18–23,26–28] an issue that has attracted widespread attention from researchers seeking improvement.

Based on these considerations, suppressing tight π–π stacking between chromophores is a practical approach to extending and enhancing solid-state photochromic performance. Supramolecular macrocyclic compounds, including crown ethers,[29,30] cyclodextrins,[31] cucurbiturils,[32,33] calixarenes,[34] and pillararenes,[35,36] offer a versatile strategy to mitigate chromophore aggregation due to their inherent cavity architectures. These macrocycles leverage non-covalent interactions (hydrogen bonding, van der Waals forces, and electrostatic interactions) and the spatial confinement of host–guest complexation to enable improved photoresponsive behavior.[37–42] For instance, encapsulation in macrocyclic cavities readily stabilizes, refines, and amplifies the optical properties of guest chromophores, encompassing photoluminescence, photochromism, and photosensitization.[43–52] Additionally, conjugating chromophores or other functional moieties to macrocyclic arene rims through covalent or coordination linkages has been extensively investigated to create advanced photoresponsive materials.[53–58]

International Joint Research Laboratory of Nano-Micro Architecture Chemistry, College of Chemistry, Jilin University, 2699 Qianjin Street, Changchun 130012, P. R. China. E-mail: ywyang@jlu.edu.cn

A rationally designed macrocycle-based photochromic material should meet the following criteria: (1) judicious selection of macrocycle type, size, and rigidity is paramount to ensure optimal spatial separation of photochromic active groups. This precise spacing is essential for robust chromic behavior, especially in the solid state, synergistically mitigating activity loss from close packing and π–π stacking. (2) Flexible electronic distributions and diverse supramolecular interactions are indispensable for facilitating chromophore twisting, bond formation, or bond cleavage, thereby optimizing the photochromic response.

Considering these criteria, pillararenes, particularly pillar[5]arenes, emerge as highly advantageous for optimizing the optical properties of photoresponsive groups.[57,59–62] Pillar[5]arenes possess a rigid, pillar-shaped structure with an exceptionally high symmetry and an optimal cavity size, which are crucial for acting as ordered scaffolds and effectively preventing active site aggregation.[63–66] Their inherent rigidity and five-fold symmetry, along with favorable synthetic yields and readily modifiable rims,[67,68] can render them ideal chromophore spacers. Moreover, the electron-rich arene units of pillar[5]arenes allow for tunable modulation of electronic distributions through delicate intermolecular interactions.[69] A practical approach to achieving this involves utilizing volatile organic compound (VOC)-induced specific superstructures, which consequently redistribute the electron density of constituent units.[51,58,69–71] This process occurs as VOCs bind to the macrocycles' internal cavities or external surfaces, a binding mechanism dictated by the VOCs' unique size, polarity, and specific intermolecular interactions. By leveraging charge-transfer or adsorption/desorption coupling, these materials can precisely regulate the microenvironment within the molecular framework, enabling or significantly amplifying phenomena such as vapochromism (vapor-induced color change) or vapoluminescence (vapor-induced luminescence change).

Herein, we present a strategy for optimizing photochromism by leveraging pillar[5]arenes as "blockers" to circumvent tight intermolecular packing and thereby enhance molecular spatial freedom. By modifying the pillar[5]arene rims with triphenylacrylonitrile (TPAN) units, we synthesized a TPAN-functionalized pillar[5]arene (**TPAN-P5**, Scheme 1a). To investigate the pillararene's crucial role in regulating photochromic activity, a control compound lacking the pillararene moiety, **TPAN-Ph** (Scheme 1a), was also prepared. Our findings reveal a remarkable contrast: **TPAN-P5** powder, when exposed to specific VOCs such as CH_3OH, HCOOH, and ethyl acetate (EA), visibly transforms into a pink hue under 365 nm light irradiation and reverts to its initial state in darkness or under white light irradiation (Scheme 1b). **TPAN-Ph** powder exhibits no observable photochromic properties under identical

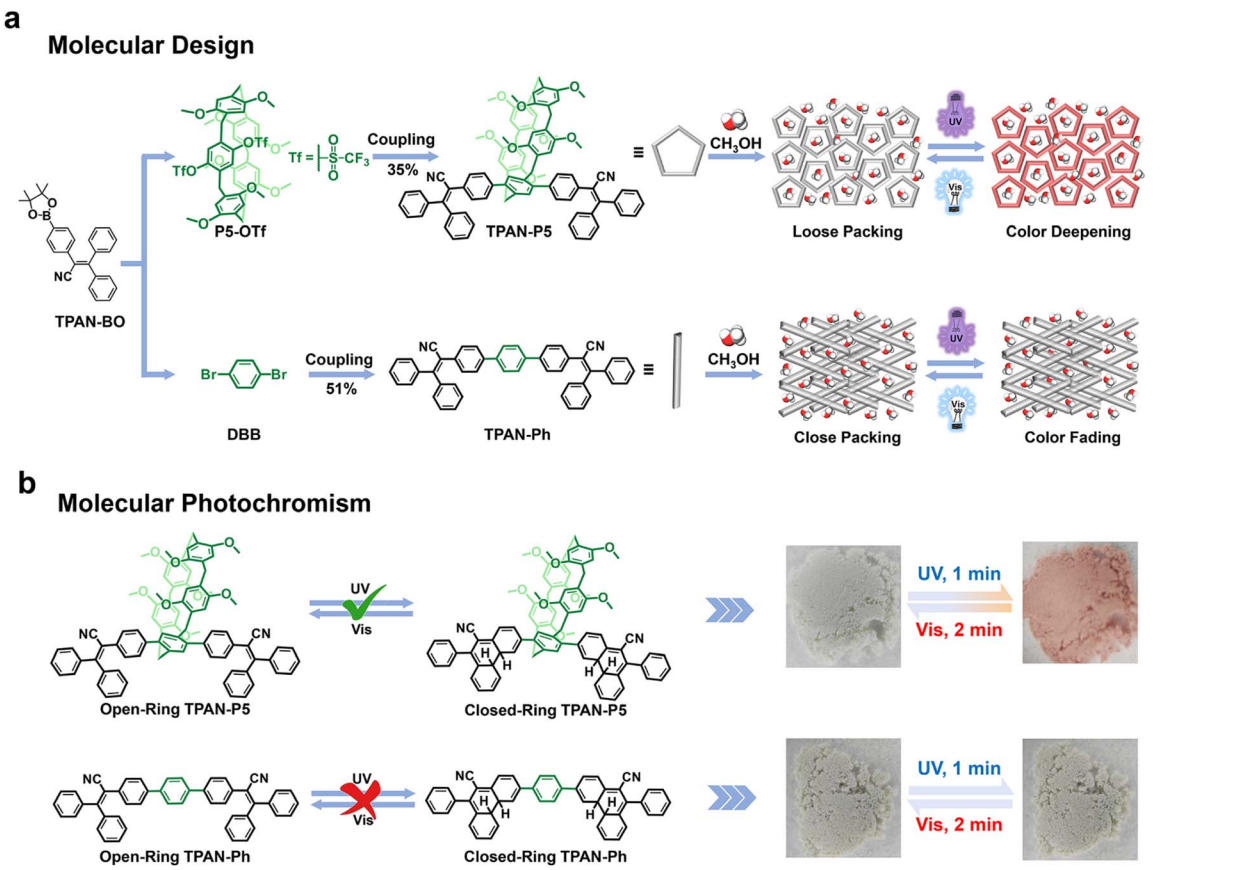

Scheme 1 (a) Schematic diagram of the molecular design and photochromic features. (b) Structural transformation and photographs of TPAN-P5 and TPAN-Ph powders before and after 365 nm light irradiation.

conditions. The photochromism observed in **TPAN-P5** is attributed to the enhanced molecular spatial freedom conferred by the pillararene cavity. This freedom optimally separates the TPAN units, effectively preventing detrimental close packing and π–π stacking. It facilitates supramolecular interactions between the TPAN units and VOCs, which, in turn, lead to the formation of stable superstructures. These supramolecular architectures significantly reconfigure the excited-state electron distribution within the TPAN chromophore, enabling free rotation and subsequent bond formation of the TPAN units, thereby powerfully promoting the solid-state photocyclization reaction. Furthermore, the multi-stimuli-responsive **TPAN-P5** powder shows excellent potential for practical applications in UV printing, anti-counterfeiting, and multi-dimensional information encryption, due to its fast response speed, anti-fatigue properties, and long color retention time.

Results and discussion

Syntheses and characterization of TPAN-P5 and TPAN-Ph

TPAN-P5 and **TPAN-Ph** were synthesized *via* a one-step Suzuki coupling reaction. The required brominated and boronated triphenylacrylonitrile derivatives (TPAN-Br and **TPAN-BO**), triflate-bearing pillar[5]arene (**P5-OTf**), and 1,4-dibromobenzene (**DBB**) were prepared according to literature procedures or purchased directly (Schemes S1–S3).[57] Both compounds were rigorously purified by column chromatography, and their chemical structures were confirmed by ^{1}H and ^{13}C nuclear magnetic resonance (NMR) spectra, high-resolution mass spectrometry (HRMS), and single-crystal X-ray diffraction (SC-XRD) (Fig. S1–S7). To elucidate the influence of the pillar[5]arene moiety on the configuration and conformation of the TPAN chromophore, single crystals of **TPAN-P5** and **TPAN-Ph** were obtained by slow solvent evaporation from mixed CH_3OH/CH_2Cl_2 and CH_3OH/$CHCl_3$ solutions, respectively, affording transparent block-shaped crystals (Table S1).

The crystal structure of **TPAN-P5**, determined to be monoclinic with space group $P2/n$, revealed that TPAN incorporation at the pillar[5]arene periphery did not substantially perturb the macrocycle's overall geometry (Fig. 1a). The cavity retained a regular pentagonal shape with a diameter of 4.7 Å, comparable to that of an unmodified pillar[5]arene.[35] The TPAN unit's benzene rings, directly linked to pillar[5]arene, exhibited a 60.19° twist relative to the macrocycle plane, adopting opposing orientations (Fig. 1b and S8). This orientation, combined with the inherent void space of the pillararene cavity, promoted a staggered, non-close-packed arrangement of neighboring **TPAN-P5** molecules. Consequently, the crystal packing featured one-dimensional channels along the *a*-axis (Fig. 1c) and a layered, staggered pattern along the *b*- and *c*-axes (Fig. S9). As expected for a photochromic TPAN derivative, the C···C distance between *cis*-oriented benzene rings was measured to be 3.378 Å (Fig. 1d), priming the molecule for photocyclization.[18] Crucially, the pillararene cavity can provide ample free volume for these photoactive TPAN moieties, as evidenced by centroid-to-centroid distances of 11.524 Å and 12.396 Å between the TPAN's benzene rings directly connected to the pillararene (Fig. 1e and f). This free volume is essential for reducing steric crowding and promoting the necessary rotation and cyclization of TPAN units, processes that are otherwise hindered by intermolecular interactions. **TPAN-Ph** crystallized in a monoclinic lattice (space group $P2_1/c$) and exhibited an intramolecular distance of 3.189 Å between *cis*-oriented benzene rings, an intramolecular arrangement theoretically suitable for photocyclization (Fig. 1g). However, unlike **TPAN-P5**, the terphenyl moiety in **TPAN-Ph** exhibited a smaller dihedral angle of only 29.58° (Fig. 1h and S10), implying enhanced conjugation that can restrict torsional motion. Furthermore, **TPAN-Ph** displayed a close-packed arrangement with rhombus-shaped pores (Fig. 1i and S11) and significantly smaller intermolecular distances between active sites (4.911, 9.142, 11.125, 4.277, and 6.170 Å; Fig. 1j–l) compared to **TPAN-P5**, highlighting a more constrained packing environment.

Photochromic properties of TPAN-P5 and TPAN-Ph in solution

The photochromic properties of **TPAN-P5** and **TPAN-Ph** were investigated in solution and solid states to assess our design strategy. Upon UV irradiation (365 nm), a **TPAN-P5** solution in CH_2Cl_2 exhibited a new absorption band at 485 nm with increasing irradiation time, accompanied by a color change from colorless to orange-red (Fig. 2a and S12). This transformation was reversible, with the solution returning to its initial state in the dark after 27 minutes (Fig. S13). Irradiation with visible light significantly accelerated the reverse reaction, completing it in just 5 minutes (Fig. 2b and S13), highlighting the light-controlled nature of the photochromism. **TPAN-Ph**, when dissolved in CH_2Cl_2, also exhibited photochromic behavior, displaying an additional absorption peak at around 500 nm (Fig. 2c and S14). Besides, **TPAN-Ph** displayed spontaneous fading in the dark (4 minutes) and accelerated fading (18 seconds) under white light irradiation (Fig. 2d and S15).

The photochromic performance of **TPAN-P5** and **TPAN-Ph** was quantified (Fig. 2e), with **TPAN-P5** showing a 3.6-fold higher conversion efficiency than **TPAN-Ph**. This enhancement is attributed to the intrinsic structural and electronic influence of pillararene. With its electron-rich, rigid cavity, pillararene optimizes the electronic landscape and molecular conformation of the TPAN unit, thereby promoting more efficient photocyclization. Moreover, the photoisomerized **TPAN-P5** showed superior stability, as evidenced by its lower spontaneous and white light-induced fading rates (Fig. S16). The recovery kinetics deviated from ideal first-order behavior, necessitating direct determination of half-lives from experimental traces. **TPAN-P5** showed significantly longer dark recovery ($t_{1/2} = 82$ s) compared to **TPAN-Ph** ($t_{1/2} = 13$ s), while white light irradiation shortened the half-lives to 36 and 7 s, respectively (Fig. 2f and S17). This has confirmed the enhanced photochromic and coloration-retention properties of **TPAN-P5** compared to **TPAN-Ph**. Moreover, **TPAN-P5** exhibited excellent cycling stability with no significant fatigue observed after six cycles, whereas **TPAN-Ph** retained only 73% of its initial coloration intensity after the first cycle (Fig. 2g, h and S18).

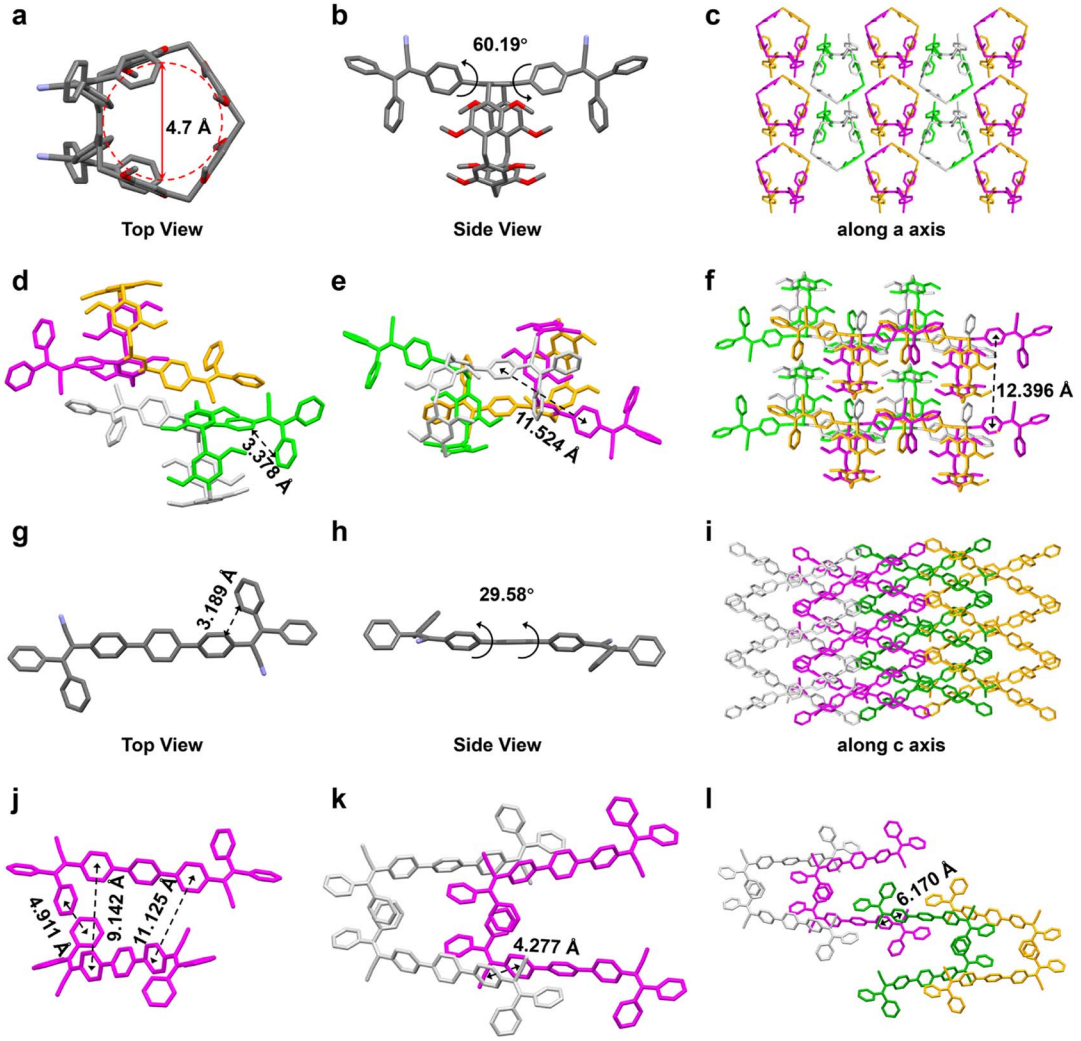

Fig. 1 (a) Top view, (b) side view, and (c) packing mode in the SC-XRD structure of **TPAN-P5**. (d) Bonding distance required for photoisomerization in the SC-XRD of **TPAN-P5**. (e and f) Distances between photochromic TPAN groups in the **TPAN-P5** crystal, measured using the connecting pillar[5]arene benzene ring. (g) Bonding distance required for photoisomerization in the SC-XRD of **TPAN-Ph**. (h) Dihedral angles and (i) packing mode of the **TPAN-Ph** crystal. (j–l) Distances between TPAN groups in the **TPAN-Ph** crystal.

The photoinduced cyclization of the TPAN unit, responsible for the photochromism of **TPAN-P5** and **TPAN-Ph** in solution, was confirmed by ^{1}H NMR spectroscopy before and after irradiation at 365 nm. The TPAN unit, as a typical photochromic group capable of photoinduced cyclization, initially cyclizes upon light irradiation to form the ring-closed isomer TPAN-B (Fig. S19).[20] Subsequently, due to TPAN-B's poor thermal stability, it readily transforms into the dehydrogenated form, TPAN-C, in air. Thus, prolonged UV irradiation of **TPAN-P5** and **TPAN-Ph** in $CDCl_3$ solution yielded the dehydrogenated species, **TPAN-P5**–C and **TPAN-Ph**–C, respectively, originating from **TPAN-P5**–B and **TPAN-Ph**–B (Fig. S20 and S21). This confirms that the photochromic mechanism of both compounds is a structural transformation caused by intramolecular cyclization. The TPAN unit endows both **TPAN-P5** and **TPAN-Ph** with aggregation-induced emission (AIE) characteristics. While **TPAN-P5** showed weak fluorescence emission at around 400 nm in tetrahydrofuran, increasing the water fraction (f_w) from 0% to 95% induced a red shift of the emission peak to 502 nm, accompanied by enhanced aggregation and a maximum fluorescence intensity at f_w = 95% (Fig. S22). **TPAN-Ph** displayed AIE, with its aggregated state exhibiting a fluorescence emission peak at 510 nm (Fig. S23). According to the CIE chromaticity diagram, **TPAN-P5** transitioned from deep blue (0.16, 0.05) to blue-green (0.19, 0.40) with increasing aggregation, while the chromaticity coordinates of **TPAN-Ph** shifted from (0.16, 0.10) to (0.21, 0.46) (Fig. S24).

To further evaluate the influence of the pillar[5]arene cavity on the photoresponsive behavior of TPAN, we investigated the photophysical and photochemical properties of the two compounds in the aggregated state. The less densely packed TPAN within **TPAN-P5** facilitated intramolecular cyclization, leading to the emergence of a new, albeit weak, absorption band at around 510 nm upon UV irradiation, a feature absent in **TPAN-Ph** (Fig. S25). Additionally, powder emission peaks were observed at 530 nm (**TPAN-P5**) and 502 nm (**TPAN-Ph**) (Fig. 2i),

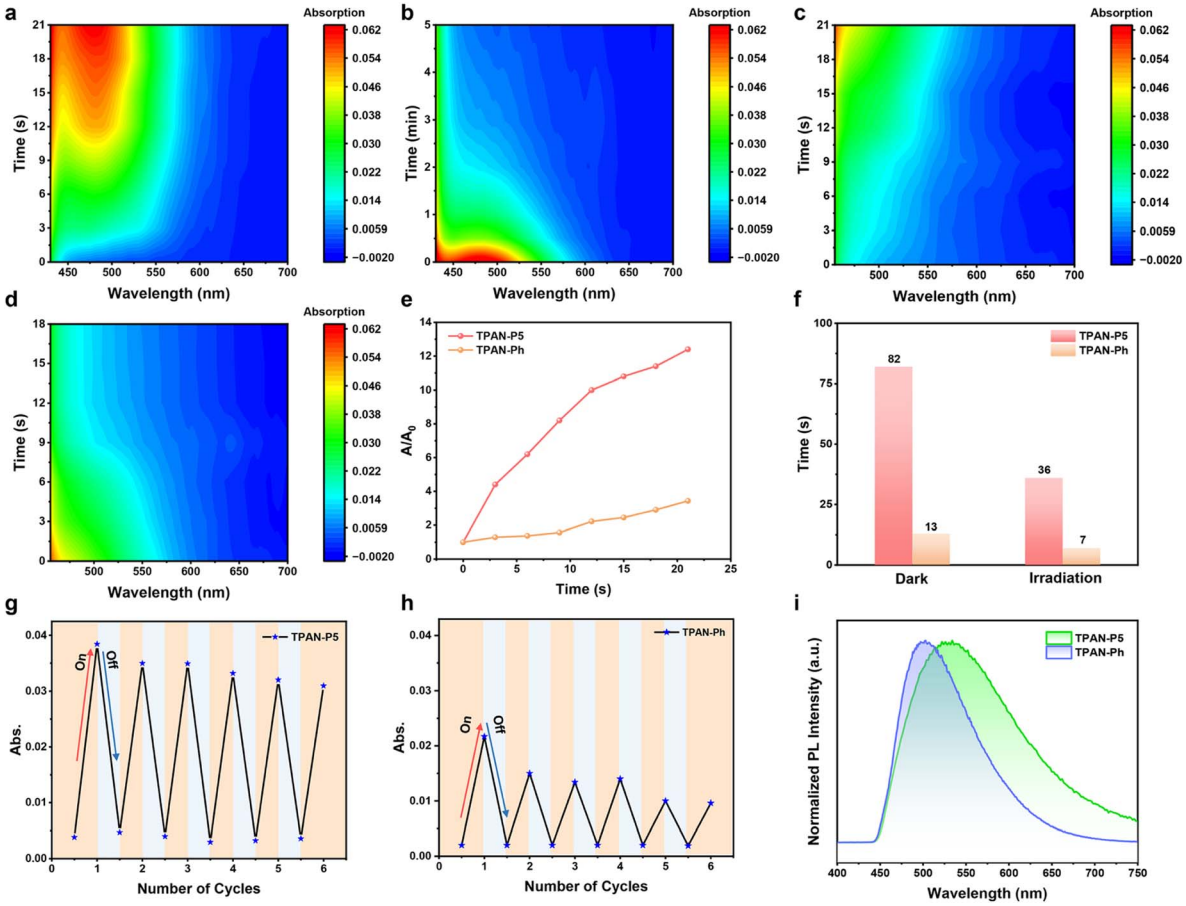

Fig. 2 Time-resolved UV-vis absorption spectra of **TPAN-P5** in CH_2Cl_2 under irradiation with (a) 365 nm light and (b) white light. Time-resolved UV-vis absorption spectra of **TPAN-Ph** in CH_2Cl_2 under irradiation with (c) 365 nm light and (d) white light. (e) Time-dependent coloration profiles of **TPAN-P5** and **TPAN-Ph** in CH_2Cl_2 under UV irradiation for different time intervals. (f) Half-lives of bleaching for **TPAN-P5** and **TPAN-Ph** in CH_2Cl_2 in the dark and under white light irradiation. Reversible switching of absorption intensity for (g) **TPAN-P5** and (h) **TPAN-Ph** in CH_2Cl_2 through 6 cycles of alternating UV (30 seconds) and visible light (5 minutes) irradiation. (i) PL spectra of **TPAN-P5** and **TPAN-Ph**.

with a lower photoluminescence quantum yield (PLQY) for **TPAN-P5** (18.74%) than for **TPAN-Ph** (27.37%) (Fig. S26). We attribute this diminished PLQY to the looser packing of TPAN in **TPAN-P5**, which facilitates intramolecular cyclization. This cyclization promotes absorption and restricts the AIE characteristics of TPAN, resulting in weaker fluorescence emission. To further validate this hypothesis, we calculated the free volume fraction (FVF) of **TPAN-P5** and **TPAN-Ph** crystals. The results revealed that **TPAN-P5** exhibited a higher FVF (35.01%) than **TPAN-Ph** (32.48%) (Fig. 3a and b). The larger FVF, correlating with a lower PLQY, suggests that the enhanced non-radiative decay pathways arising from vibrational relaxation in fluorescence emission provide more energy for photoinduced cyclization.

The electronic structure was further investigated using frontier orbital analysis based on density functional theory (DFT) calculations, aiming to elucidate how pillararenes promote the photocyclization of TPAN. In **TPAN-P5**, the highest occupied molecular orbital (HOMO, −5.58 eV) is predominantly localized on the pillararene framework, while the lowest unoccupied molecular orbital (LUMO, −1.97 eV) resides on the TPAN unit (Fig. 3c). This clear spatial separation establishes a distinct donor–acceptor partitioning, which supports a directional intramolecular charge-transfer (ICT) pathway upon excitation. Conversely, in **TPAN-Ph**, both the HOMO (−5.58 eV) and LUMO (−1.97 eV) are extensively co-localized across the entire molecular framework (Fig. 3d), indicating that its lowest-energy excitation is highly delocalized in nature. This suggests that **TPAN-P5**, owing to its ICT character, undergoes a substantial change in dipole moment upon photoexcitation, which, in turn, acts as a potent driving force to induce significant intramolecular charge polarization and concomitant structural rearrangements, thereby establishing optimal conditions for subsequent cyclization. Moreover, this notable dipole moment difference also renders the excited state particularly sensitive to solvent polarity. The resulting solvatochromic stabilization may drastically reduce the excited-state energy, consequently modulating both the reaction pathway and its activation barrier. In contrast, **TPAN-Ph**, upon delocalized excitation, shows a negligible change in dipole moment, lacks these advantageous attributes, and exhibits poor photocyclization efficiency. Additionally, owing to the ICT character induced by

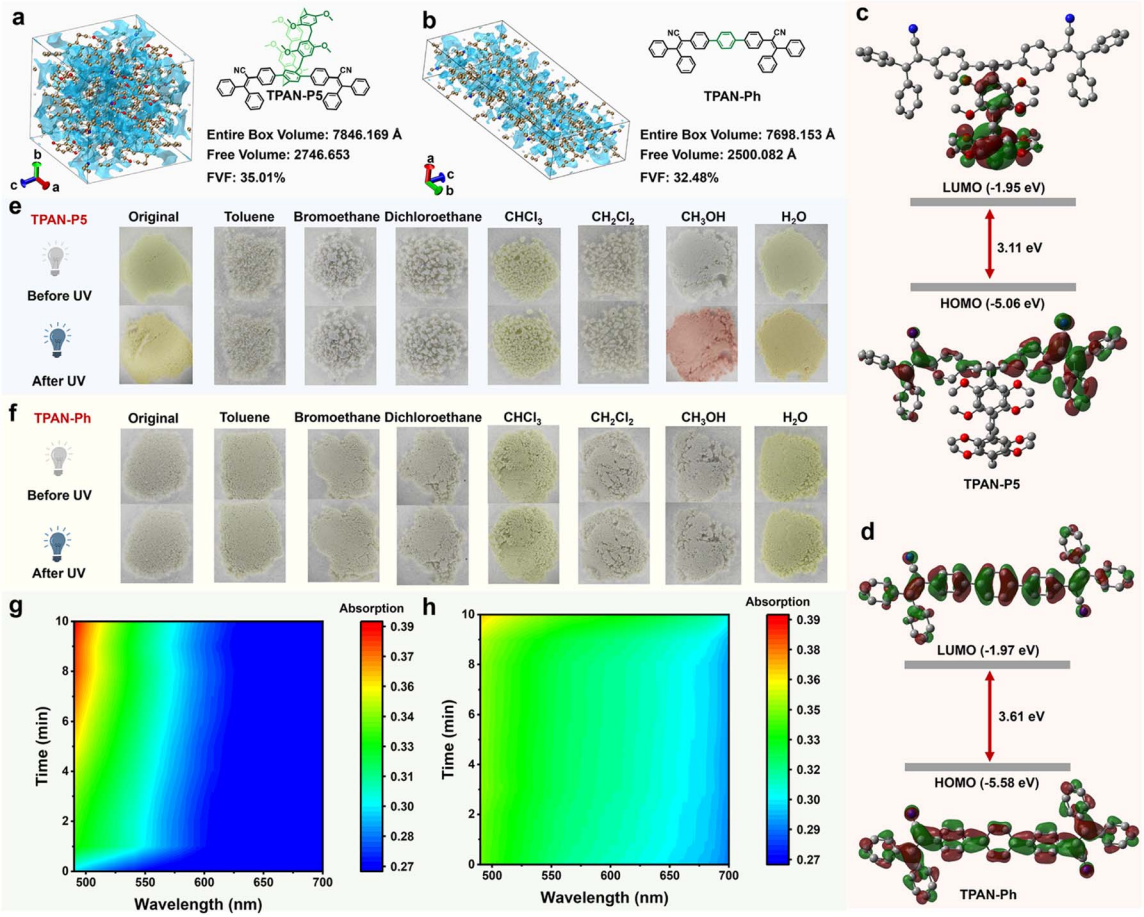

Fig. 3 The FVF of (a) **TPAN-P5** and (b) **TPAN-Ph**. HOMO and LUMO distributions of (c) **TPAN-P5** and (d) **TPAN-Ph**. Color photographs of various VOC-fumigated (e) **TPAN-P5** and (f) **TPAN-Ph** powders before and after 1 minute of 365 nm light irradiation. Time-resolved UV-vis absorption spectra of (g) **TPAN-P5**–CH_3OH and (h) original **TPAN-P5** powders under 365 nm light irradiation.

the pillar[5]arene acting as an electron donor, the excited-state lifetime of **TPAN-P5** (7.5 ns) is considerably longer than that of **TPAN-Ph** (0.9 ns), thereby providing ample time for the cyclization to proceed (Fig. S27).

VOC-dependent photochromic behaviors of TPAN-P5 *versus* TPAN-Ph in the solid state

Considering the susceptibility of **TPAN-P5**'s large excited-state dipole moment to solvent polarity, various VOCs (such as toluene, bromoethane, 1,2-dichloroethane, $CHCl_3$, CH_2Cl_2, CH_3OH, CH_3CH_2OH, and H_2O) were selected to promote TPAN cyclization, thereby further enhancing its photochromic performance in the aggregated state. Remarkably, only CH_3OH vapor, under 365 nm UV irradiation, induced a pronounced pink coloration in **TPAN-P5** powder, accompanied by a characteristic absorption peak at 510 nm in its UV-vis spectrum (Fig. 3e and S28). Furthermore, the ^1H NMR spectrum of the CH_3OH-fumigated **TPAN-P5** (**TPAN-P5**–CH_3OH) powder after 10 minutes of photoirradiation provided clear evidence of cyclization (Fig. S29). **TPAN-P5**–CH_3OH powder exhibited reversible photochromism, reverting from pink to white upon exposure to white light (Fig. S30). In contrast, **TPAN-Ph** powder showed no photochromic response in analogous experiments, due to a negligible change in its excited-state dipole moment (Fig. 3f), indicating inhibited solid-state photocyclization. Similarly, exposure of the solid TPAN-Br monomer to CH_3OH vapor did not induce coloration (Fig. S31). UV-vis absorption spectroscopy kinetics studies revealed the crucial influence of CH_3OH on the photochromic behavior of **TPAN-P5**. Upon irradiation with 365 nm light, the **TPAN-P5**–CH_3OH powder exhibited a significant and sustained enhancement of the absorption band in the 490–700 nm region within only ten minutes (Fig. 3g and S32). In stark contrast, the original **TPAN-P5** powder lacked any noticeable dynamic changes in absorption under the same conditions (Fig. 3h and S32). Further kinetic analysis indicated that the **TPAN-P5**–CH_3OH powder faded slowly in the dark, whereas visible-light irradiation significantly accelerated this fading (Fig. S33). Conversely, the original **TPAN-P5** powder exhibited no measurable kinetic response under either dark or visible light conditions (Fig. S34).

VOC-selective solid-state photochromism of TPAN-P5

To investigate the scope of this vapor-dependent photochromism, a broader range of VOCs was tested, such as acids, bases,

aldehydes, ketones, and cycloalkanes. Among the various VOCs examined, only HCOOH, in addition to CH_3OH, induced a visually discernible, amplified photochromic transformation from white to pink in the **TPAN-P5** powder (Fig. S35). This transformation was also reversible upon visible light irradiation (Fig. S36). Other VOCs did not exhibit a comparable effect on **TPAN-P5** photocyclization, showing only weak color changes, similar to those observed for the original **TPAN-P5** powder (Fig. S37). Solid-state UV-vis absorption spectra of **TPAN-P5** powders fumed with these other VOCs showed no significant peak or band at 510 nm (Fig. S38). Correspondingly, ^{1}H NMR spectra also lacked characteristic signals for the cyclized product (Fig. S39). Furthermore, analogous to CH_3OH-fumed **TPAN-Ph** and TPAN-Br powders, HCOOH also failed to enhance the aggregated-state photochromic ability of these compounds (Fig. S40), highlighting the necessity of the pillar-shaped cavities.

To further define the characteristics of these VOCs, a range of alcohols and acids was examined. Remarkably, while CH_3OH and HCOOH readily facilitated **TPAN-P5** photocyclization, other alcohols and acids with larger molecular sizes (including CH_3-CH_2OH, ethylene glycol, 1,2-propanediol, isopentanol, isobutanol, and acetic acid (HAc)) did not yield such a stable pink color change or a distinct spectroscopic signature (Fig. S41 and S42). This compelling observation strongly suggests that the VOC-induced photochromism of **TPAN-P5** powder is not solely determined by interactions with VOC molecules. Instead, synergistic effects involving both the geometric size and the precise electronic influence of the VOCs are essential.

Synergy between intermolecular interactions and structural order in solid-state photochromism of TPAN-P5

Building upon the observed VOC-dependent photochromism, we hypothesize that matched molecular dimensions enable specific VOCs to efficiently intercalate into specific microenvironments within the **TPAN-P5** aggregates (*e.g.*, micropores or interfacial voids), rather than simply forming disordered aggregates. Concurrently, the intrinsic dipole moments of the VOC molecules, through the induction of local microenvironmental electric fields, fine-tune the electronic structure and energy-level distribution of **TPAN-P5**. This concerted effect ultimately generates an optimal molecular conformation and electronic state conducive to an efficient photocyclization reaction under 365 nm light excitation. To validate this hypothesis, we exposed **TPAN-P5** powder to CH_3OH vapor and monitored the resulting color change *via* photography at various exposure times (Fig. 4a). Simultaneously, we quantified the CH_3OH content in the powder to correlate adsorption with photochromic behavior. Appreciable photochromism was observed in **TPAN-P5** after only 0.5 hours of CH_3OH adsorption, with no significant increase in intensity after 5 hours of continued exposure. ^{1}H NMR spectra of these powders in $CDCl_3$ revealed a new signal at 3.48 ppm, attributable to the $-CH_3$ protons of CH_3OH (Fig. S43). While the chemical shift of the $-CH_3$ protons remained constant with increasing exposure time, the signal exhibited splitting, suggesting intermolecular interactions between CH_3OH and **TPAN-P5**. Moreover, based on a CH_3OH content of 0.60 mol per mol of **TPAN-P5** (Fig. S44), we have further inferred that CH_3OH is unlikely to be tightly encapsulated within the **TPAN-P5** cavity.

Additionally, powder X-ray diffraction (PXRD) measurements were performed on **TPAN-P5** powders treated with various VOCs to investigate whether VOC-induced changes in the packing mode significantly influence the photochromic properties (Fig. S45). The PXRD patterns revealed distinct crystalline phases in **TPAN-P5** upon exposure to CH_3OH and HCOOH, both of which are known to induce photochromism. Specifically, **TPAN-P5**–CH_3OH powder exhibited a crystalline phase corresponding to the thermodynamically stable packing of crystalline **TPAN-P5**. In contrast, this stable phase was not observed in the powder exposed to HCOOH. Furthermore, while cyclohexane- and triethylamine-fumigated **TPAN-P5** powders showed weak reflections indicative of a packing mode similar to that of the thermodynamically stable phase, no visible pink coloration was observed. Additionally, the absence of visible pink coloration in the amorphous **TPAN-P5** powder obtained by grinding underscores the importance of structural organization (Fig. S45 and S46). These results suggest that, while not dictated by a specific crystalline packing mode, photochromism of **TPAN-P5** is facilitated by the order within the framework, presumably because it provides the necessary molecular environment, including sufficient spatial freedom, for photochromic transformation.

To distinguish the respective roles of CH_3OH-mediated intermolecular interactions and structural order in the photochromism of **TPAN-P5** powder, **TPAN-P5**–CH_3OH powder was subjected to sequential heating at elevated temperatures (110, 120, and 130 °C) for a total of 72 hours. ^{1}H NMR analysis revealed the presence of residual CH_3OH after heating (Fig. S47), indicating strong intermolecular interactions between CH_3OH and **TPAN-P5**. Remarkably, despite the significant loss of CH_3OH and the consequent disruption of long-range order (Fig. S48), the heated powder retained detectable photochromic activity (Fig. S49). This sharply contrasts with the amorphous **TPAN-P5** powder obtained by mechanical grinding, as mentioned earlier, which showed no photochromism. The critical divergence lies in the presence of residual CH_3OH in the heated sample, which sustains intermolecular interactions even in a disordered state. These results demonstrate that CH_3OH-derived intermolecular interactions are indispensable for initiating the photochromic response, while structural order primarily serves as a secondary enhancer, facilitating more effective CH_3OH anchoring and the spatial arrangement of reactive sites. In light of the preceding analysis, the robust photochromism of **TPAN-P5** is fundamentally attributed to the spatial freedom provided by its molecular pillar-shaped cavities. Structurally, the pillararene component serves as a spatial "blocker", hindering close packing of TPAN moieties and generating voids around the reactive sites. Within these voids, CH_3OH molecules may establish hydrogen bonds or other dipole–dipole interactions that promote the formation of reversible covalent bonds between adjacent benzene rings within the TPAN moiety.

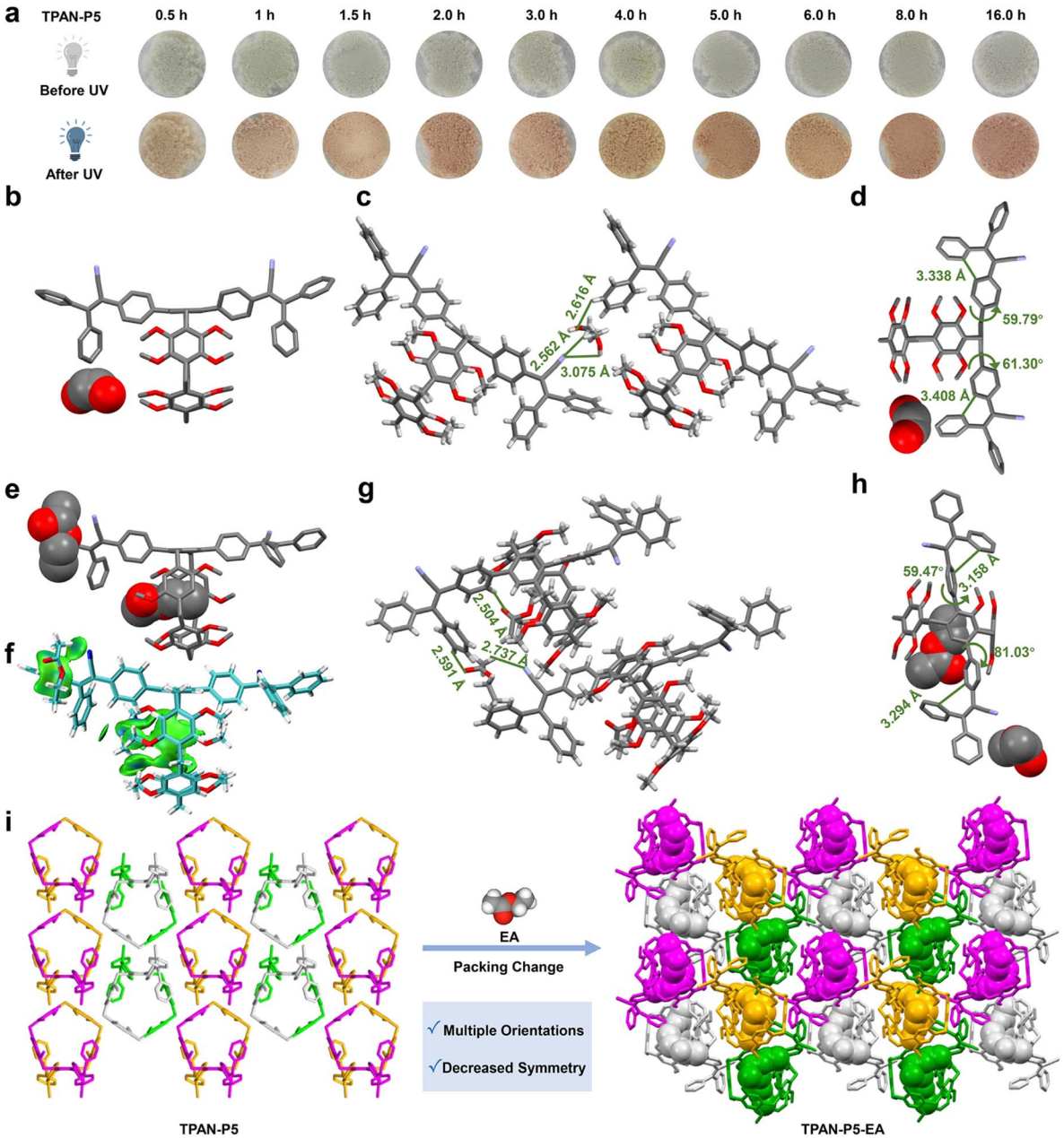

Fig. 4 (a) Time-dependent photographs of **TPAN-P5** obtained before and after UV irradiation after exposure to CH_3OH. (b) SC-XRD structure of **TPAN-P5**–CH_3OH. (c) C–H···N (2.562 Å), C–H···O (2.616 Å), and O–H···N (3.075 Å) interactions between **TPAN-P5** and CH_3OH. (d) Bonding distances required for photoisomerization and dihedral angles of the terphenyl moiety in the **TPAN-P5**–CH_3OH co-crystal. (e) SC-XRD structure of **TPAN-P5**–EA. (f) Binding iso-surfaces between **TPAN-P5** and the EA complex. (g) C–H···N (2.737 Å) and C–H···O (2.591 Å and 2.504 Å) interactions between **TPAN-P5** and EA. (h) Bonding distances required for photoisomerization and dihedral angles of the terphenyl moiety in the **TPAN-P5**–EA co-crystal. (i) Packing modes of **TPAN-P5** and **TPAN-P5**–EA crystals.

Structural basis of VOC-mediated pre-reactive conformations for photocyclization

TPAN-P5–CH_3OH co-crystals (Table S2) were prepared and characterized using a synchrotron radiation source to further refine the function of CH_3OH. Consistent with the ^1H NMR data for **TPAN-P5**–CH_3OH powder, disordered CH_3OH molecules surrounded the TPAN moiety at the end of **TPAN-P5** without penetrating the cavity (Fig. 4b, the disordered CH_3OH is shown with two possible orientations). C–H···N (2.562 Å), C–H···O (2.616 Å), and O–H···N (3.075 Å) interactions existed between CH_3OH and the **TPAN-P5** molecule (Fig. 4c). The terphenyl unit exhibited twist angles of 59.79° and 61.30° (Fig. 4d and S50), with distances of 3.338 and 3.408 Å between the bonding benzene rings in the **TPAN-P5**–CH_3OH crystal, which are geometrically conducive to the photoisomerization reaction. This confirms that CH_3OH mediates the formation of a pre-reactive conformation of **TPAN-P5** through polar intermolecular interactions, thereby facilitating initial photoinduced cyclization.

To further validate this mechanism of conformation induction, we sought to grow additional photochromic crystals with improved structural clarity. We selected ethyl acetate (EA), a suitable **TPAN-P5** solvent, as a functional substitute for CH_3OH. EA-fumigated **TPAN-P5** (**TPAN-P5**–EA) powder resulted in a pink color change upon 365 nm UV irradiation (Fig. S51 and S52). The lack of chemical shift changes in **TPAN-P5** and EA, coupled with an EA : **TPAN-P5** adsorption stoichiometry of 1.38 : 1 (Fig. S53), supports an EA-induced photochromic mechanism in **TPAN-P5**, analogous to that of CH_3OH. The complete abolition of photochromism upon thermal removal of EA at 110 °C (Fig. S54), coupled with the restoration of ordered **TPAN-P5** packing (Fig. S55), further demonstrates that the photochromism in **TPAN-P5**–EA powder, much like that in **TPAN-P5**–CH_3OH powder, stems from the intermolecular interactions between EA and **TPAN-P5** molecules.

TPAN-P5–EA co-crystals were further cultured to investigate the specific intermolecular interactions that promote aggregated-state photochromism (Table S2 and Fig. S56). EA molecules were found within the pentagonal cavity of **TPAN-P5** and in the space surrounding the TPAN group (Fig. 4e). To further estimate and visualize the weak interactions between EA and **TPAN-P5**, we performed an independent gradient model (IGM) analysis. The resulting **TPAN-P5**–EA binding iso-surfaces (green and blue regions in Fig. 4f and S57) revealed weak interactions concentrated not only at the electron-deficient guest edge within the cavity, but also at reactive TPAN sites, such as the cyclizing benzene rings and the cyano group. Further structural analysis indicated that EA formed numerous weak interactions with **TPAN-P5**, as we had anticipated. These interactions primarily arise from C–H$\cdots\pi$ (3.103 Å), C–H$\cdots$N (2.737 Å), and C–H$\cdots$O (2.591 Å and 2.504 Å) forces between **TPAN-P5** and EA (Fig. 4g and S58). Consequently, the dihedral angles between TPAN and the pillararene were measured to be 59.47° and 81.03°, with corresponding distances between the bonding benzene rings of TPAN of 3.158 and 3.294 Å (Fig. 4h). These suitable dihedral angles and short distances between the bonding benzene rings ensure photochromism. Moreover, the incorporation of EA into the crystal matrix led to discernible multiple orientations of **TPAN-P5** (Fig. 4i) and triggered a space group transformation from the highly symmetric $P2/n$ to the less symmetric $P2_1/n$ (Tables S1 and S2). These structural changes, driven by specific supramolecular interactions, collectively induced an electronic rearrangement in TPAN, thereby facilitating the photocyclization reaction.

To elucidate the structural factors governing VOC-induced photochromism in **TPAN-P5**, we determined and compared the crystal structures of **TPAN-P5** co-crystallized with non-photochromic CH_3CH_2OH and CH_3COOH (**TPAN-P5**–CH_3CH_2OH and **TPAN-P5**–CH_3COOH) and with photochromic CH_3OH and EA. **TPAN-P5** molecules in **TPAN-P5**–CH_3CH_2OH and **TPAN-P5**–CH_3COOH co-crystals exhibited a distorted conformation. The pillararene cavity contracted, transitioning from an approximate five-fold to an asymmetric symmetry (Fig. 5a and b), a form distinct from the conformations observed in CH_3OH and EA-induced crystals. Conversely, in **TPAN-P5**–CH_3CH_2OH and **TPAN-P5**–CH_3COOH co-crystals, **TPAN-P5** molecules adopted a staggered packing that lacks the continuous one-dimensional channels found in the CH_3OH and EA systems (Fig. 5c–f).

Taking the **TPAN-P5**–CH_3CH_2OH co-crystal as an example, we define the TPAN moiety with the smaller terphenyl dihedral angle (53.89°) as 'proximal TPAN' (closer to the macrocycle) and the one with the larger dihedral angle (59.15°) as 'distal TPAN' (further from the macrocycle) (Fig. 5g and S59). Although the bonding distances between the reactive arene rings (3.314 and 3.283 Å) met preorganization criteria, the proximal TPAN was sterically hindered by the pillararene cavity. This hindering conformation was further stabilized by short C–H$\cdots$N (2.656 Å) and C–H$\cdots$O (2.585 and 2.637 Å) contacts with neighboring **TPAN-P5** molecules (Fig. 5h–j and S59). Collectively, these factors impede the arene torsion and inward adjustment required for cyclization. The packing pattern and unit cell parameters of the **TPAN-P5**–CH_3COOH co-crystal are highly similar to those of the **TPAN-P5**–CH_3CH_2OH co-crystal (Table S2, **TPAN-P5**–CH_3COOH lattice parameters: $a = 45.8868$ Å, $b = 13.1150$ Å, $c = 33.8049$ Å, $\alpha = 90°$, $\beta = 132.234°$, $\gamma = 90°$; **TPAN-P5**–CH_3CH_2OH lattice parameters: $a = 45.8525$ Å, $b = 13.1186$ Å, $c = 33.5659$ Å, $\alpha = 90°$, $\beta = 132.1990°$, $\gamma = 90°$). Within this crystal packing context, **TPAN-P5** molecules formed multiple intermolecular C–H$\cdots$O (2.638 and 2.609 Å) and C–H$\cdots$N (2.665 Å) interactions. This dense packing, mediated by these interactions, inhibits cyclization by restricting the necessary structural reorganization (Fig. S60).

We used S_1-state natural transition orbital (NTO) calculations on the four VOC-induced **TPAN-P5** conformers to explain how configuration affects photochromism at the electronic level. Upon excitation, all four conformers can transfer electrons from the electron-rich cavity to the flanking TPAN units (Fig. 5k–n). Increased electron density on the TPAN units is a prerequisite for bond formation, with unhindered TPAN twisting being a necessary condition. In the symmetric CH_3OH- and EA-induced **TPAN-P5** conformers, the excited-state electron-rich TPAN units are free from steric hindrance by the pillar-shaped cavity, enabling unimpeded twisting and bond formation and resulting in photochromism in the aggregated state. Conversely, the twisted conformations of the CH_3CH_2OH- and CH_3COOH-exposed **TPAN-P5** lead to excited-state electron localization predominantly on the proximal TPAN unit. The pillar-shaped cavity shields this TPAN unit, preventing free twisting and thus inhibiting photochromism.

Material applications

TPAN-P5's multi-stimuli-response, rapid photoresponse, and anti-fatigue properties make it suitable for UV printing, anti-counterfeiting, and information encryption. To test its use in UV printing, we created a transparent poly(methyl methacrylate) (PMMA) film with a 2 wt% **TPAN-P5** doping ratio and a thickness of 0.7 μL mm^{-2} (Fig. S61), which provided optimal photochromic performance. The film was then used in a UV printing test: a plastic stencil was placed on it, and the exposed area was irradiated with 365 nm light for 10 seconds. The areas not covered by the stencil turned a readily visible pink color,

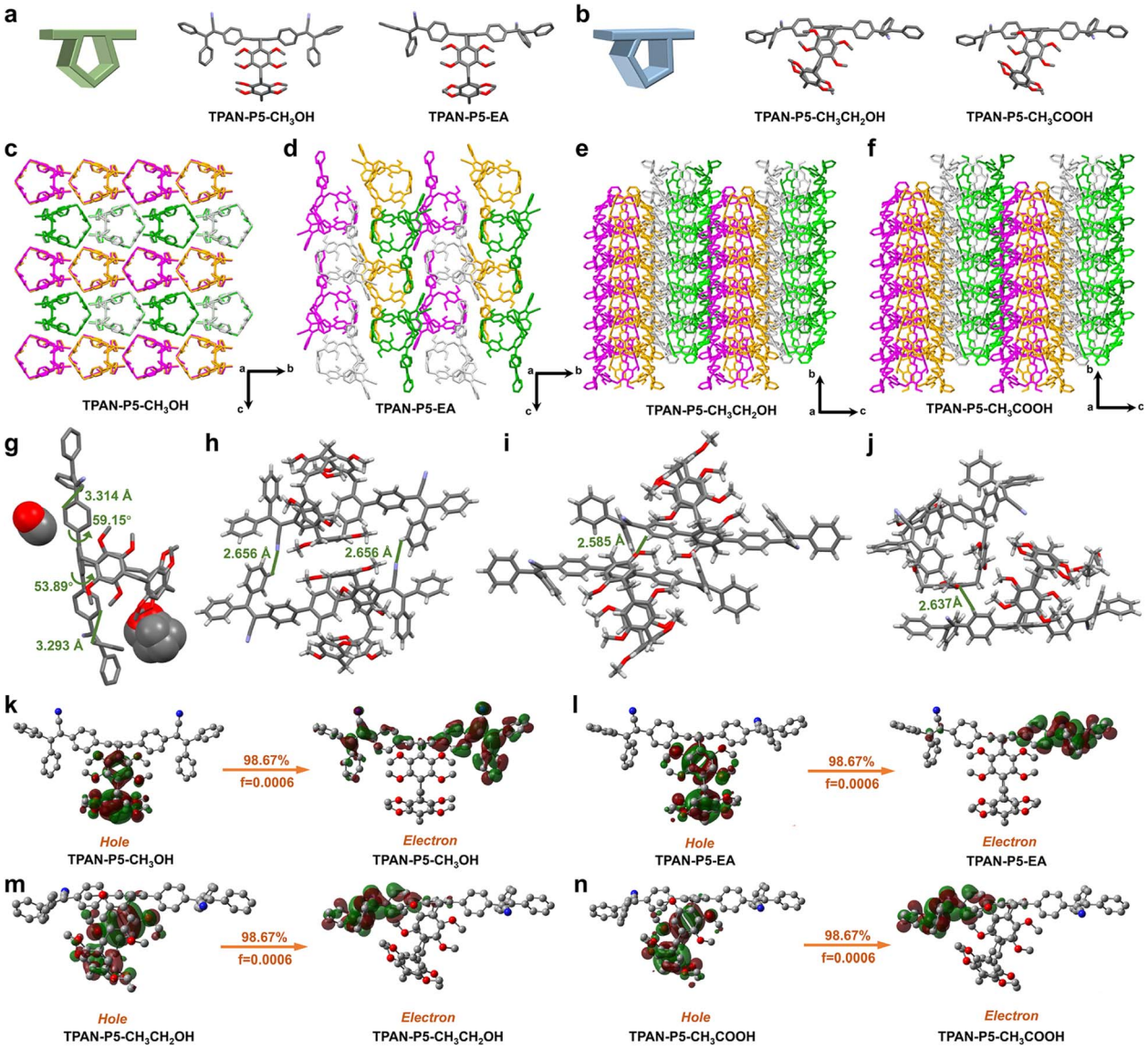

Fig. 5 (a) Side view of the SC-XRD structures of **TPAN-P5**–CH_3OH and **TPAN-P5**–EA. (b) Side view in the SC-XRD structures of **TPAN-P5**–CH_3CH_2OH and **TPAN-P5**–CH_3COOH. Packing modes of (c) **TPAN-P5**–CH_3OH, (d) **TPAN-P5**–EA, (e) **TPAN-P5**–CH_3CH_2OH, and (f) **TPAN-P5**–CH_3COOH co-crystals. (g) Dihedral angles of the **TPAN-P5**–CH_3CH_2OH co-crystal. Intermolecular (h) C–H···N (2.656 Å) and (i and j) C–N···O (2.585, 2.637 Å) interactions in the **TPAN-P5**–CH_3CH_2OH co-crystal. NTO analyses of (k) **TPAN-P5**–CH_3OH, (l) **TPAN-P5**–EA, (m) **TPAN-P5**–CH_3CH_2OH, and (n) **TPAN-P5**–CH_3COOH co-crystals.

while the covered regions remained unchanged. Furthermore, the film could be returned to its initial state within seconds upon exposure to white light, allowing for continued information input and editing using a UV light source (Fig. 6a). Utilizing the erasable nature of the **TPAN-P5**-containing PMMA film, pink "dog paw" and "shamrock" patterns were printed.

The visually discernible, delayed fading observed under ambient daylight further enhances its practical applicability (Fig. 6b). **TPAN-P5** powder exhibits a remarkable photochromic behavior that can be switched "on" and "off" by exposure to CH_3OH, suggesting its applicability for anti-counterfeiting. As illustrated in Fig. 6c, we fabricated a white "dog paw" model using **TPAN-P5** powder, with some areas exposed to CH_3OH vapor and others left untreated. Upon UV irradiation, the regions treated with CH_3OH vapor exhibited a readily discernible pink color, while the remaining areas retained white. The photochromic area can be precisely controlled by adjusting the amount of CH_3OH-fumed powder applied. This method's excellent spatial resolution was demonstrated by selectively changing the color of a paw print from one "toe" to two. This suggests that **TPAN-P5** powder could be used as an on-demand anti-counterfeiting marker on items such as banknotes, passports, ID cards, and packaging to enhance consumer and public safety.

Although QR codes are a popular choice for quick information access, thanks to their high storage capacity and rapid

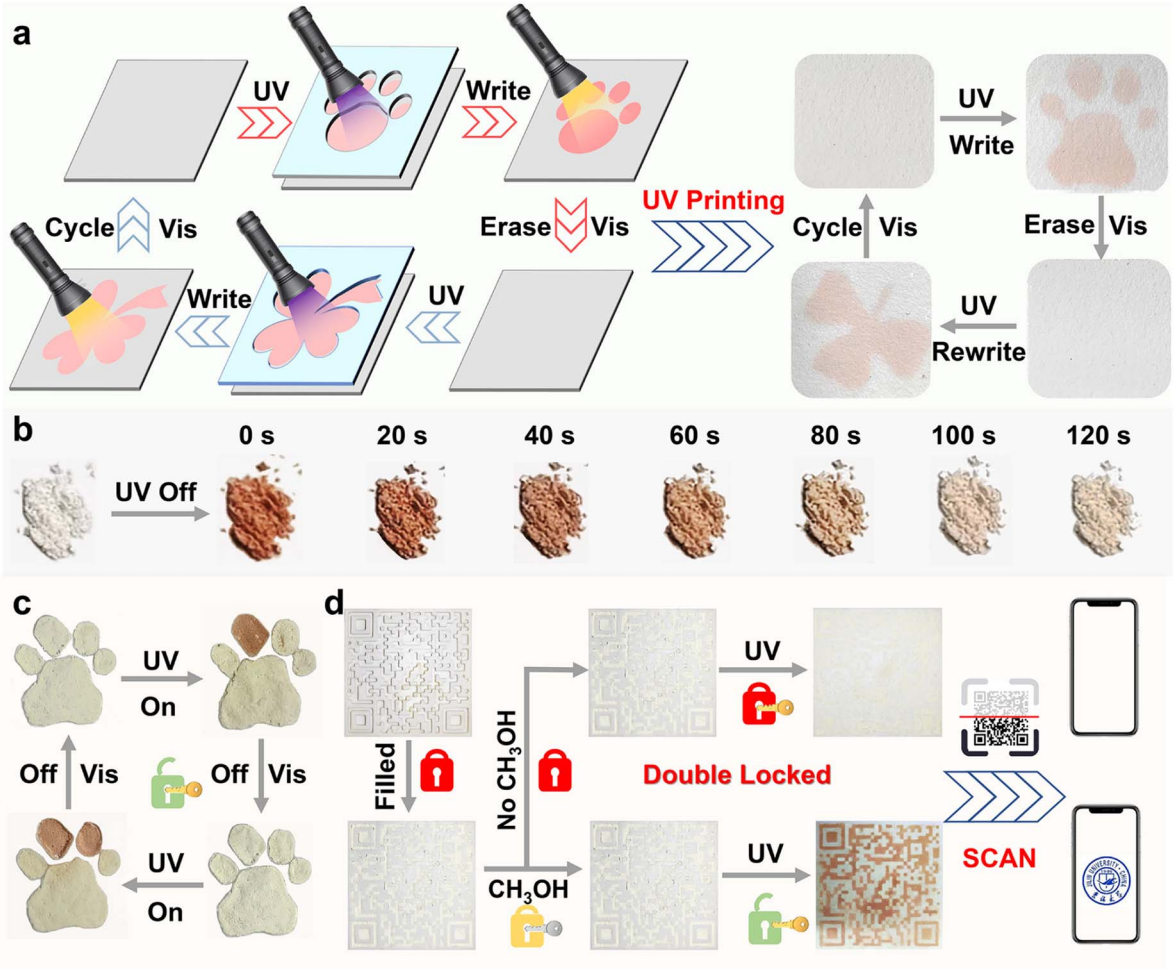

Fig. 6 (a) UV-printing process for the **TPAN-P5** photochromic film. (b) Color photographs of **TPAN-P5**–CH_3OH powder showing time-dependent bleaching under daylight after 1 minute of UV irradiation. (c) Anti-counterfeiting process for **TPAN-P5** and **TPAN-P5**–CH_3OH powders. (d) Information encryption process implemented using QR codes made with **TPAN-P5** powder.

readability,[28,72,73] many encryption applications require data to be concealed or delayed, a limitation of the technology. **TPAN-P5** powder addresses these challenges by exhibiting a significant color change, prolonged bleaching times, and sustained color retention only when exposed to specific VOC vapors and UV light. This dual-activation mechanism, attributed to multiple layers of information encryption, enhances information security. A 3D-printed white QR code was rendered active by filling it with **TPAN-P5** powder and exposing it to CH_3OH fumes (Fig. 6d). Upon 365 nm UV irradiation, the QR code rapidly turned pink, revealing its embedded information—a Jilin University logo that could be scanned with a mobile phone. The QR code was non-functional without the fuming process.

Conclusions

In summary, we described a pillararene-based strategy for enhancing molecular free volume, leading to the development of **TPAN-P5**, a macrocyclic arene with pronounced photochromic properties. **TPAN-P5** amplifies the photoisomerization characteristics of the TPAN chromophore, exhibiting superior photochromism and color retention compared to **TPAN-Ph** and the isolated chromophore itself. The pillararene cavity in **TPAN-P5** generates a larger TPAN torsional angle, disrupting π–π stacking and creating molecular free volume that facilitates both photoisomerization and VOC intercalation. This, coupled with **TPAN-P5**'s prominent ICT effect, resulting in a significant dipole moment difference between its excited and ground states, renders **TPAN-P5** powder selectively susceptible to VOC-induced photochromism *via* superstructure formation. Mechanistically, polar interactions between VOCs and **TPAN-P5** increase TPAN electron density, promoting TPAN's twisting and bond formation, thereby enabling solid-state photochromism. These molecular characteristics render **TPAN-P5** a promising candidate for applications in UV printing, anti-counterfeiting, and multiple information encryption. This work highlights the potential of pillararenes as molecular property amplifiers, offering valuable insights for the design of photochromic molecules and the advancement of macrocyclic arene applications.

Author contributions

M.-H. L. and Y.-W. Y. conceived this project and designed the experiments. M.-H. L., H. H., and Y. W. conducted the experiments. M.-H. L. drafted the work. Y.-W. Y. revised and finalised the manuscript. All authors approved the submitted version.

Conflicts of interest

There are no conflicts to declare.

Data availability

The data supporting this article are available in the SI file, which includes experimental procedures, spectroscopic and crystallographic data, photophysical characterization, and computational details. See DOI: https://doi.org/10.1039/d5sc08539j.

CCDC 2379600, 2379605, 2380579, 2448876, 2488767 and 2488768 contain the supplementary crystallographic data for this paper.[74a–f]

Acknowledgements

The authors acknowledge the National Natural Science Foundation of China (No. 22571119) and the Key Research and Development Project of the Natural Science Foundation of Jilin Province (No. 20260203095SF) for financial support. We thank the staff of the Shanghai Synchrotron Radiation Facility (SSRF) and the User Experiment Assist System for their expert support during data acquisition.

Notes and references

1 Y. Kobayashi and J. Abe, *Chem. Soc. Rev.*, 2022, **51**, 2397–2415.
2 T. Zhang, X.-Y. Lou, X. Li, X. Tu, J. Han, B. Zhao and Y.-W. Yang, *Adv. Mater.*, 2023, **35**, 2210551.
3 G. Berkovic, V. Krongauz and V. Weiss, *Chem. Rev.*, 2000, **100**, 1741–1754.
4 N. Tamai and H. Miyasaka, *Chem. Rev.*, 2000, **100**, 1875–1890.
5 N. F. König, D. Mutruc and S. Hecht, *J. Am. Chem. Soc.*, 2021, **143**, 9162–9168.
6 H. Tian and S. Yang, *Chem. Soc. Rev.*, 2004, **33**, 85–97.
7 C.-L. Wong, M. Ng, E. Y.-H. Hong, Y.-C. Wong, M.-Y. Chan and V. W.-W. Yam, *J. Am. Chem. Soc.*, 2020, **142**, 12193–12206.
8 D. J. Wales, Q. Cao, K. Kastner, E. Karjalainen, G. N. Newton and V. Sans, *Adv. Mater.*, 2018, **30**, 1800159.
9 M. Estrader, J. S. Uber, L. A. Barrios, J. Garcia, P. Lloyd-Williams, O. Roubeau, S. J. Teat and G. Aromí, *Angew. Chem., Int. Ed.*, 2017, **56**, 15622–15627.
10 R. C. Shallcross, P. O. Körner, E. Maibach, A. Köhnen and K. Meerholz, *Adv. Mater.*, 2013, **25**, 4807–4813.
11 Y. Yang, J. He, Z. He and G. Jiang, *Adv. Opt. Mater.*, 2021, **9**, 2001584.
12 S. N. Corns, S. M. Partington and A. D. Towns, *Color. Technol.*, 2009, **125**, 249–261.
13 J. Lott, C. Ryan, B. Valle, J. R. Johnson iii, D. A. Schiraldi, J. Shan, K. D. Singer and C. Weder, *Adv. Mater.*, 2011, **23**, 2425–2429.
14 Z. Li, X. Zeng, C. Gao, J. Song, F. He, T. He, H. Guo and J. Yin, *Coord. Chem. Rev.*, 2023, **497**, 215451.
15 C. Jia, A. Migliore, N. Xin, S. Huang, J. Wang, Q. Yang, S. Wang, H. Chen, D. Wang, B. Feng, Z. Liu, G. Zhang, D.-H. Qu, H. Tian, M. A. Ratner, H. Q. Xu, A. Nitzan and X. Guo, *Science*, 2016, **352**, 1443–1445.
16 M. Li and W.-H. Zhu, *Acc. Chem. Res.*, 2022, **55**, 3136–3149.
17 H.-B. Cheng, S. Zhang, E. Bai, X. Cao, J. Wang, J. Qi, J. Liu, J. Zhao, L. Zhang and J. Yoon, *Adv. Mater.*, 2022, **34**, 2108289.
18 Z. Xiong, X. Zhang, L. Liu, Q. Zhu, Z. Wang, H. Feng and Z. Qian, *Chem. Sci.*, 2021, **12**, 10710–10723.
19 D. Zhang, Y. Zhang, W. Gong, J. Li, S. Liu, Y. Ma and Q. Zhao, *Adv. Opt. Mater.*, 2023, **11**, 2300386.
20 D. Ou, T. Yu, Z. Yang, T. Luan, Z. Mao, Y. Zhang, S. Liu, J. Xu, Z. Chi and M. R. Bryce, *Chem. Sci.*, 2016, **7**, 5302–5306.
21 Y. Fan, M. Han, A. Huang, Q. Liao, J. Tu, X. Liu, B. Huang, Q. Li and Z. Li, *Mater. Horiz.*, 2022, **9**, 368–375.
22 M. Luo, J. Zhao, Q. Yan, C. Li, Y. Liu, Z. Yang, Z. Mao, S. Wang and Z. Chi, *Chem. Eng. J.*, 2024, **499**, 156214.
23 Y. Xiao, M. Shen, J. Li, H. Wang, H. Sun, Y. He, R. Huang, T. Yu and W. Huang, *Adv. Funct. Mater.*, 2024, **34**, 2312930.
24 Y. Xiao, J. Li, Z. Song, J. Liao, M. Shen, T. Yu and W. Huang, *J. Am. Chem. Soc.*, 2025, **147**, 20372–20380.
25 Z. Xie, X. Zhang, Y. Xiao, H. Wang, M. Shen, S. Zhang, H. Sun, R. Huang, T. Yu and W. Huang, *Adv. Mater.*, 2023, **35**, 2212273.
26 T. J. White, in *Photomechanical Materials, Composites, and Systems*, ed. T. J. White, John Wiley & Sons, Inc., Hoboken, NJ, 2017, pp. 393–403.
27 D. E. Williams, C. R. Martin, E. A. Dolgopolova, A. Swifton, D. C. Godfrey, O. A. Ejegbavwo, P. J. Pellechia, M. D. Smith and N. B. Shustova, *J. Am. Chem. Soc.*, 2018, **140**, 7611–7622.
28 G. Huang, Q. Xia, W. Huang, J. Tian, Z. He, B. S. Li and B. Z. Tang, *Angew. Chem., Int. Ed.*, 2019, **58**, 17814–17819.
29 Z. Liu, S. K. M. Nalluri and J. F. Stoddart, *Chem. Soc. Rev.*, 2017, **46**, 2459–2478.
30 J. Li, D. Yim, W.-D. Jang and J. Yoon, *Chem. Soc. Rev.*, 2017, **46**, 2437–2458.
31 M. T. Sikder, M. M. Rahman, M. Jakariya, T. Hosokawa, M. Kurasaki and T. Saito, *Chem. Eng. J.*, 2019, **355**, 920–941.
32 Y.-H. Liu, Y.-M. Zhang, H.-J. Yu and Y. Liu, *Angew. Chem., Int. Ed.*, 2021, **60**, 3870–3880.
33 R. D. Mukhopadhyay and K. Kim, *Nat. Chem.*, 2023, **15**, 438.
34 C. D. Gutsche, *Acc. Chem. Res.*, 1983, **16**, 161–170.
35 T. Ogoshi, S. Kanai, S. Fujinami, T.-a. Yamagishi and Y. Nakamoto, *J. Am. Chem. Soc.*, 2008, **130**, 5022–5023.
36 M. Xue, Y. Yang, X. Chi, Z. Zhang and F. Huang, *Acc. Chem. Res.*, 2012, **45**, 1294–1308.
37 T. Ogoshi, T.-a. Yamagishi and Y. Nakamoto, *Chem. Rev.*, 2016, **116**, 7937–8002.
38 H. Ju, C. N. Zhu, H. Wang, Z. A. Page, Z. L. Wu, J. L. Sessler and F. Huang, *Adv. Mater.*, 2022, **34**, 2108163.

39 T. Ogoshi, S. Takashima and T.-a. Yamagishi, *J. Am. Chem. Soc.*, 2018, **140**, 1544–1548.
40 H. Nie, Z. Wei, X.-L. Ni and Y. Liu, *Chem. Rev.*, 2022, **122**, 9032–9077.
41 Z. Liu and Y. Liu, *Chem. Soc. Rev.*, 2022, **51**, 4786–4827.
42 X.-Y. Lou, S. Zhang, Y. Wang and Y.-W. Yang, *Chem. Soc. Rev.*, 2023, **52**, 6644–6663.
43 A. Blanco-Gómez, P. Cortón, L. Barravecchia, I. Neira, E. Pazos, C. Peinador and M. D. García, *Chem. Soc. Rev.*, 2020, **49**, 3834–3862.
44 G. Wu and Y.-W. Yang, *Cell Rep. Phys. Sci.*, 2024, **5**, 101873.
45 C.-M. Yu, X. Meng, X. Liu, Z.-Y. Zhang and C. Li, *Chem. Mater.*, 2022, **34**, 358–365.
46 S. Song, H. Zhang and Y. Liu, *Acc. Mater. Res.*, 2024, **5**, 1109–1120.
47 X.-H. Wang, N. Song, W. Hou, C.-Y. Wang, Y. Wang, J. Tang and Y.-W. Yang, *Adv. Mater.*, 2019, **31**, 1903962.
48 Y. Qin, X. Liu, P.-P. Jia, L. Xu and H.-B. Yang, *Chem. Soc. Rev.*, 2020, **49**, 5678–5703.
49 P. Spenst, R. M. Young, B. T. Phelan, M. Keller, J. Dostál, T. Brixner, M. R. Wasielewski and F. Würthner, *J. Am. Chem. Soc.*, 2017, **139**, 2014–2021.
50 Y.-D. Yang, X.-L. Chen, J. Liang, J.-W. Fang, J. L. Sessler and H.-Y. Gong, *J. Am. Chem. Soc.*, 2023, **145**, 14010–14018.
51 J. Huang, H. Feng, L. Zhang and K. Jie, *Angew. Chem., Int. Ed.*, 2025, **64**, e202500022.
52 K. Omoto, S. Tashiro and M. Shionoya, *J. Am. Chem. Soc.*, 2021, **143**, 5406–5412.
53 M.-H. Li, C. Xu and Y.-W. Yang, *Coord. Chem. Rev.*, 2024, **512**, 215894.
54 X.-Y. Lou, G. Zhang, M.-H. Li and Y.-W. Yang, *Nano Lett.*, 2023, **23**, 1961–1969.
55 M.-H. Li, Z. Yang, H. Hui, B. Yang, Y. Wang and Y.-W. Yang, *Angew. Chem., Int. Ed.*, 2023, **62**, e202313358.
56 Z. Li, Z. Yang, Y. Zhang, B. Yang and Y.-W. Yang, *Angew. Chem., Int. Ed.*, 2022, **61**, e202206144.
57 Q. Li, Y. Wu, J. Cao, Y. Liu, Z. Wang, H. Zhu, H. Zhang and F. Huang, *Angew. Chem., Int. Ed.*, 2022, **61**, e202202381.
58 Q. Li, H. Zhu and F. Huang, *J. Am. Chem. Soc.*, 2019, **141**, 13290–13294.
59 Z. Li and Y.-W. Yang, *Adv. Mater.*, 2022, **34**, 2107401.
60 H. Zhu, Q. Li, W. Zhu and F. Huang, *Acc. Mater. Res.*, 2022, **3**, 658–668.
61 X.-Y. Lou, G. Zhang, N. Song and Y.-W. Yang, *Biomaterials*, 2022, **286**, 121595.
62 C.-L. Song, Z. Li, J.-R. Wu, T. Lu and Y.-W. Yang, *Chem. Mater.*, 2022, **34**, 10181–10189.
63 H. Zhang, Z. Liu, F. Xin and Y. Zhao, *Coord. Chem. Rev.*, 2020, **420**, 213425.
64 G. Zhang, B. Hua, A. Dey, M. Ghosh, B. A. Moosa and N. M. Khashab, *Acc. Chem. Res.*, 2021, **54**, 155–168.
65 Z.-Q. Wang, X. Wang and Y.-W. Yang, *Adv. Mater.*, 2024, **36**, 2301721.
66 Y. Wu, L. Shi, L. Xu, J. Ying, X. Miao, B. Hua, Z. Chen, J. L. Sessler and F. Huang, *Nature*, 2025, **640**, 676–682.
67 H. Zhang, Z. Liu and Y. Zhao, *Chem. Soc. Rev.*, 2018, **47**, 5491–5528.
68 T.-H. Shi, S. Ohtani, K. Kato, S. Fa and T. Ogoshi, *Trends Chem.*, 2023, **5**, 537–550.
69 J.-R. Wu, G. Wu, D. Li and Y.-W. Yang, *Angew. Chem., Int. Ed.*, 2023, **62**, e202218142.
70 Y.-K. Zhu, A. Liu, G. Wu, L. Yuan, Y.-H. Jin, M.-H. Li, X. Wang and Y.-W. Yang, *Angew. Chem., Int. Ed.*, 2025, e202513299.
71 D. Zou, Z. Li, D. Long, X. Dong, H. Qu, L. Yang and X. Cao, *ACS Appl. Mater. Interfaces*, 2023, **15**, 13545–13553.
72 S. Dong, Q. Zang, Z.-Y. Ma, M. Tang, Z.-K. Xu, J. Nie, B. Du, J. Z. Sun and B. Z. Tang, *ACS Appl. Mater. Interfaces*, 2022, **14**, 17794–17805.
73 P. Carou-Senra, L. Rodríguez-Pombo, A. Awad, A. W. Basit, C. Alvarez-Lorenzo and A. Goyanes, *Adv. Mater.*, 2024, **36**, 2309164.
74 (*a*) CCDC 2379600: Experimental Crystal Structure Determination, 2026, DOI: 10.5517/ccdc.csd.cc2kw59y; (*b*) CCDC 2379605: Experimental Crystal Structure Determination, 2026, DOI: 10.5517/ccdc.csd.cc2kw5g3; (*c*) CCDC 2380579: Experimental Crystal Structure Determination, 2026, DOI: 10.5517/ccdc.csd.cc2kx5wk; (*d*) CCDC 2448876: Experimental Crystal Structure Determination, 2026, DOI: 10.5517/ccdc.csd.cc2n6805; (*e*) CCDC 2488767: Experimental Crystal Structure Determination, 2026, DOI: 10.5517/ccdc.csd.cc2pjrtt; (*f*) CCDC 2488768: Experimental Crystal Structure Determination, 2026, DOI: 10.5517/ccdc.csd.cc2pjrvv.